Ⓔ

Coseismic and Initial Postseismic Deformation from the 2004 Parkfield, California, Earthquake, Observed by Global Positioning System, Electronic Distance Meter, Creepmeters, and Borehole Strainmeters

by J. Langbein, J. R. Murray, and H. A. Snyder

Abstract   Global Positioning System (GPS), electronic distance meter, creepmeter, and strainmeter measurements spanning the **M** 6.0 Parkfield, California, earthquake are examined. Using these data from 100 sec through 9 months following the mainshock, the Omori's law, with rate inversely related to time, $1/t^p$ and p ranging between 0.7 and 1.3, characterizes the time-dependent deformation during the postseismic period; these results are consistent with creep models for elastic solids. With an accurate function of postseismic response, the coseismic displacements can be estimated from the high-rate, 1-min sampling GPS; and the coseismic displacements are approximately 75% of those estimated from the daily solutions. Consequently, fault-slip models using daily solutions overestimate coseismic slip. In addition, at 2 months and at 8 months following the mainshock, postseismic displacements are modeled as slip on the San Andreas fault with a lower bound on the moment exceeding that of the coseismic moment.

Online material: Data description and supplementary figures, tables, and data used in models and time-series analysis.

Introduction

The 2004 **M** 6.0 Parkfield, California, earthquake occurred within a dense network of 14 continuously operating Global Positioning System (CGPS) receivers, 12 creepmeters, 7 borehole strainmeters, and 13 electronic distance meter (EDM) baselines that span the rupture zone of this earthquake (Fig. 1). Following the earthquake, the U.S. Geological Survey (USGS) deployed additional survey-mode GPS (SGPS) receivers at 32 other sites in the region to augment the spatial coverage of CGPS observations of deformation for this earthquake. Both Langbein *et al.* (2005) and Savage *et al.* (2005) present the initial observations and their interpretations. Since the coseismic and postseismic deformation is large relative to the errors in the data, these data should provide constraints for various aspects of the coseismic, postseismic, and the interseismic periods of the earthquake cycle. This article concentrates on our analysis of deformation during the initial postseismic period.

One of the key observations from the 2004 Parkfield earthquake is the amount of postseismic deformation (Figs. 2 and 3). Significant, postseismic deformation was also observed for the 1966 Parkfield earthquake (Scholz *et al.*, 1969, Smith and Wyss, 1968). In contrast to the observations made for the 1966 event, our observations start within seconds after the 2004 mainshock and, because we had a large

network of crustal deformation instruments already installed with the purpose of observing Parkfield earthquakes (Roeloffs and Langbein, 1994), we can analyze a data set with vastly greater spatial and temporal coverage than available for 1966. In particular, the CGPS data are important to the problem of postseismic deformation because of their good temporal resolution derived from 1-sec estimates of position (Bock *et al.*, 2000; Larson *et al.*, 2003) and their excellent long-term stability (Williams *et al.*, 2004). The CGPS data are augmented both by borehole strainmeter data, creepmeter data, and two-color EDM data. Although both the strain and creep data have much better precision than GPS over short time intervals, their long-term precision is reduced relative to GPS. Finally, the SGPS observations improve our spatial coverage of deformation.

With these observations, this report examines three aspects of the deformation. Our primary focus is to characterize the time dependence of these data. Initially, this is done through the application of Omori's Law, where the rate of deformation is inversely proportional to the time following the mainshock. This simple function has been successfully applied to studies of aftershock rates (e.g., Reasenberg and Jones, 1989). With Omori's law there is no physical relationship that is described. On the other hand, other physical
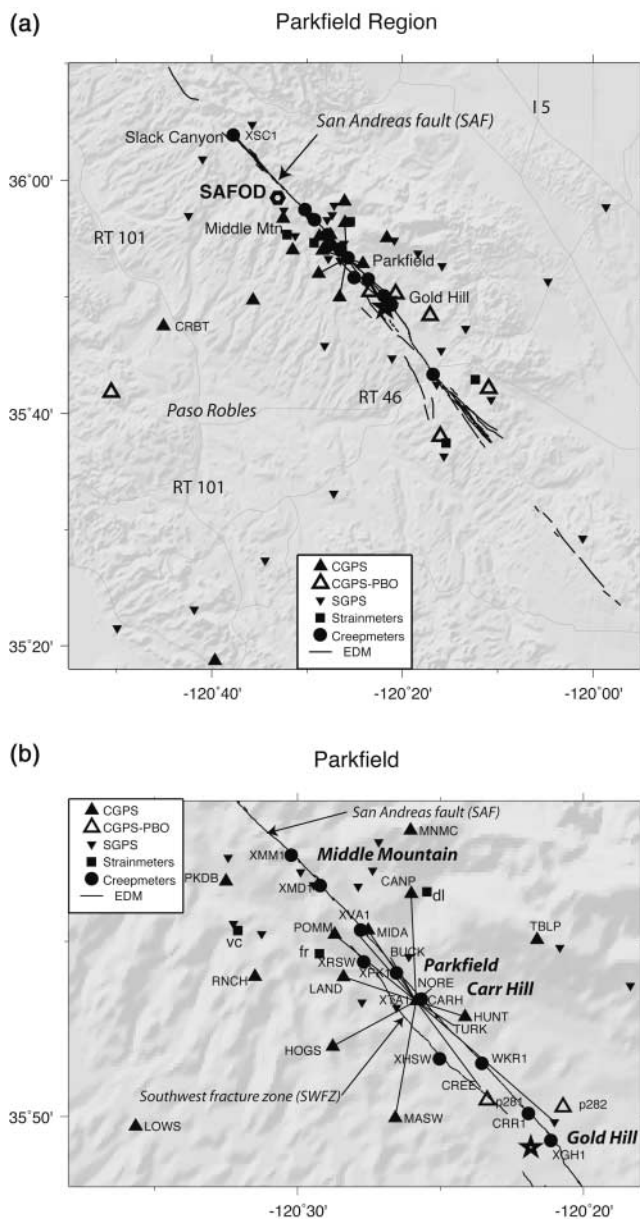
Figure 1. Locations of GPS, EDM, creepmeters, and borehole strainmeters in the Parkfield region and their relative locations to the San Andreas fault. Topography is shown as a gray scaled, shaded relief. Major highways and towns are labeled. (a) Broad Parkfield region and the locations of all of the instrumentation discussed in this report are shown. The geographic points, Slack Canyon, Middle Mountain, Parkfield, and Gold Hill are located. The star is location of the epicenter of the 28 September **M** 6.0 Parkfield earthquake. (b) Locations of CGPS, creepmeters, EDM, and strainmeters near the town of Parkfield are shown. The rupture zone of the 2004 earthquake extends the length of the fault shown in b.

models, including those proposed by Marone *et al.* (1991), Perfettini and Avouac (2004), and Montési (2004) approximate Omori's Law in functional form. Secondly, since postseismic deformation begins immediately after the mainshock (Fig. 2) and is large within the first day following the mainshock, the actual estimate of amount of coseismic deformation depends upon the temporal character of the deformation immediately after the mainshock. In the absence of high-rate solutions, the initial postseismic signal would be aliased and, consequently, the estimate of the coseismic offset would be biased. Finally, after estimating the coseismic offsets for the CGPS data and examining the extensive SGPS observations, we can estimate the distribution of slip during and following the Parkfield mainshock.

We conclude that through the initial 8 months of observations, a modified form of Omori's law (Jeffreys, 1958; Utsu, 1961), where rate is proportional to $1/t^p$, fits both the CGPS and the creepmeter observations. Extrapolation of Omori's law suggests that postseismic deformation will continue for the next 5 to 10 years, assuming continued aseismic slip or creep of the San Andreas fault. Although the strainmeter data have some of the temporal characteristics of Omori's law, those data suggest that other mechanisms might operate. Second, because of the high rate of postseismic deformation immediately following the Parkfield earthquake, slip models that are based upon daily observation of GPS positions tend to overestimate the moment of the earthquake, a feature noted by Langbein *et al.* (2005), where the moment estimated from seismic data is about 70% of that using only geodetic measurements. Here, by using the high-rate GPS data, our estimate of the coseismic moment for the 2004 Parkfield earthquake is consistent with estimates using seismic data. Finally, through modeling the GPS data during the initial eight months of the postseismic period, the moment of the postseismic slip exceeds the moment of the coseismic slip.

Data

Four different sets of crustal deformation data are examined: GPS, two-color EDM, creepmeters, and borehole strainmeters (Fig. 1). The GPS data are used throughout this report because of both their greater temporal and spatial sampling. Thus, most of this section concerns the processing of the GPS data to achieve the best precision. (Ⓔ See also the material available in the electronic edition of BSSA.)

In many of the steps required to process these data, we have assumed a time-dependent signal in a time series of the data is as follows:

$$d_i = D_o + Rt_i + S\sin(2\pi ft_i) + C\cos(2\pi ft_i)$$
$$\text{for } t_i < T_{eq} \quad (1)$$
$$= D_o + Rt_i + S\sin(2\pi ft_i) + C\cos(2\pi ft_i)$$
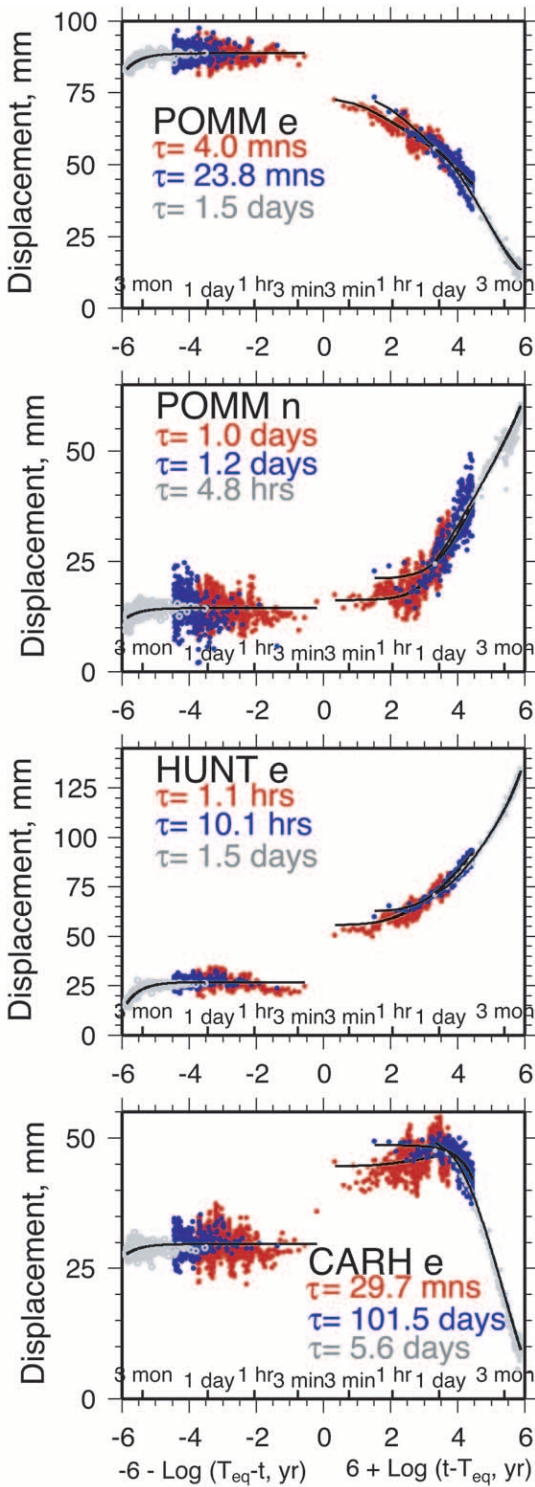$$+ O + A\log(1 + (t_i - T_{eq})/\tau) \text{ for } t_i \geq T_{eq},$$

Figure 2.   Observed displacements versus modeled displacements for four CGPS sites relative to CRBT. The time axis is in log(T) centered about the time of the earthquake. The lines represent the fit (equation 1) of the simplified Omori's law and an offset to these data. The data for each site are plotted with different sampling rates; the red is 1-min samples, blue is 30-min samples, and gray is 1-day samples. The corresponding values of τ for each time series are indicated. The last panel shows the displacement record for CARH, which coseismically displaced to the southeast, but for most of the postseismic period, it displaced to the northwest.
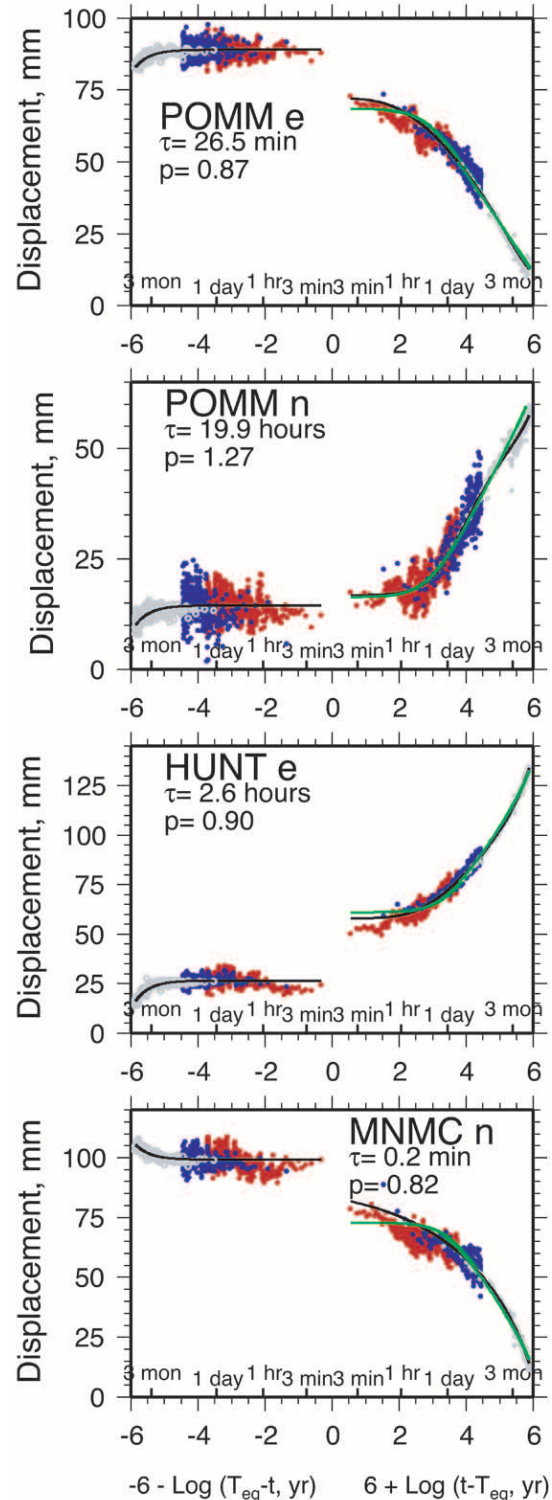
Figure 3.   Observed displacements versus modeled displacements for CGPS sites relative to CRBT. See Figure 2 for explanation of symbols. The black line represents the fit of the modified Omori's law (equation 2) to the data and the green line is the fit of the model proposed by Perfettini and Avouac (2004). The values of τ and index, p, of the modified Omori's law for baseline are indicated.

where the observation, d_i, is made at time t_i, and T_{eq} is the time of the mainshock, D_o is a nominal value of the observation, R is the rate, O is the coseismic offset, A is the amplitude of a simplified Omori's law with τ being the time constant, and C and S are the amplitude of a periodic component with frequency f. The sinusoidal function arises from an annual periodicity seen in many data sets from Parkfield. With borehole strain, however, the sinusoidal term is actually a collection of the tidal constituents; thus several of the diurnal and semidiurnal terms are required. The rate, R, is the background interseismic rate; and the postseismic deformation, represented by Omori's law, is superimposed upon the background rate. The time constant, τ, in Omori's law can be viewed as the time delay of the onset of postseismic deformation following the mainshock; τ is not a relaxation time.

GPS

GPS data have been collected in two modes. First, 14 sites (CGPS) in the Parkfield region are permanently located and continuously collect data (Fig. 1) (Langbein and Bock, 2004). At 13 sites these data are collected once per second; the fourteenth site records data at 30-sec intervals. These sites were installed between 1996 and 2001 and, for the most part, have taken over the monitoring of crustal deformation that had been done with two-color EDM since 1986 (Langbein *et al.*, 1990; Roeloffs and Langbein, 1994)

Within two days of the mainshock on 28 September 2004, the USGS occupied 13 more sites in the Parkfield region. These sites have had previous occupations since 1992, and their last occupation prior to the 2004 event was in mid-2003. Between late September and late November 2004, GPS receivers were left to collect data in a semicontinuous mode. Finally, between mid-April and mid-May 2005, the 13 sites were reoccupied, and 19 more had their first occupation since the Parkfield earthquake. All of these measurements are considered as campaign style, SGPS, measurements.

Following the 2004 Parkfield earthquake, the Plate Boundary Observatory (PBO) (http://pboweb.unavco.org) established five more continuously operating GPS sites in the greater Parkfield area. These additional sites are located south and southeast of the Parkfield CGPS stations and serve to augment the spatial coverage of CGPS on the fault southeast of the Parkfield segment.

Monuments used for most of the CGPS sites are the deeply braced design that are drilled into the ground surface 8 to 10 deep (Langbein *et al.*, 1995). In contrast, the SGPS sites use traditional geodetic monuments, including buried cement blocks, rock outcrops, and pipe driven to refusal.

The data from the CGPS sites have been processed in two modes. The first mode produces a single position estimate for each site for each day using point positioning in the GPS inferred positioning system (Zumberge *et al.*, 1997). The second mode uses the method of Bock *et al.* (2000) to estimate the position once per second of each site relative to

POMM, which lies adjacent to the fault (Fig. 1). A limitation of Bock's method is that, unlike point positioning, it cannot estimate absolute displacements. In order to better observe both the coseismic and the postseismic deformation, the displacements were reestimated relative to a site farthest from the fault, CRBT, using simple subtraction rather than reprocessing the raw phase data. This was done for both the daily solutions and the 1-Hz solutions. Although there are other 1-Hz, CGPS sites farther from the fault than CRBT, these sites are in southern California and are too far away to achieve high precision positions using the method of Bock *et al.* (2000).

The raw 1-Hz displacements were further processed iteratively to remove outliers, to improve precision, and to decimate. Precision was improved by using a sidereal filter (Langbein and Bock, 2004), and by stacking similar components of the displacement time series to find the common mode signals for the east, north, and vertical components (Wdowinski *et al.*, 1997). Additionally, because many of the GPS sites recorded seismic waves, the observations for the 100 sec after the earthquake were deleted. To reduce the number of observations for analysis, the data were decimated to 1-min samples for the 12 hr centered on the time of the Parkfield mainshock and decimated to 3-min samples for the remaining 4 days centered on the earthquake. Additionally, these 1-sec data were decimated to 30-min samples for a 20-day period centered on the earthquake. Details of this algorithm are included ⒺE in the electronic edition of BSSA.

Examples of time series with 1-min, 30-min, and 24-hr sampling for a few of the sites are shown in Figures 2 and 3. With the high-sample-rate data, these data can have periods of extensive wander. One such example of wander seen in Figures 2 and 3 is the 1-min data from the north component of POMM for the 1-hr period that encompasses the earthquake. In part, some of the wander could be due to multipath interference that is not corrected by the processing of the 1-Hz data. In fact, detailed analysis by K. Larson (personal comm., 2005) indicates that a number of the Parkfield sites experience significant multipath interference.

EDM

The two-color EDM network (Langbein, 2004, Slater and Huggett, 1976) was established in the mid-1980s to monitor the deformation of the Parkfield region in anticipation of a Parkfield earthquake (Langbein *et al.*, 1990; Roeloffs and Langbein, 1994). With the installation of CGPS by 2001, which included many common sites with the EDM, the EDM measurements became less important, and the monitoring of length changes was tapered from a few times each week to a few times each year. Furthermore, the number of baselines was also reduced from 17 to 13. Prior to the 2004 event, the EDM network was measured in April 2004. Following the Parkfield earthquake, 12 of the 13 baselines were measured approximately two to four times in late November and early December 2004. And, coincident with the

more extensive SGPS measurements in spring 2005, all of the EDM baselines were measured two to four times.

Creepmeters

Twelve creepmeters are in the Parkfield region; 10 of the sites are on the San Andreas fault and 2 are on the southwest fracture zone (SWFZ). The creepmeter network (Roeloffs and Langbein, 1994, Schulz, 1989) had its first sites installed immediately following the 1966 Parkfield earthquake (Smith and Wyss, 1968). The network gradually grew to 12 stations by the mid-1980s. The creepmeter uses an Invar wire to measure the change in distance between two piers located on either side of the surface trace of the fault. It is assumed that the change in distance measured by the extensometer is due to slip on the fault that the meter straddles. The distance between the piers is typically 30 m, and these piers are 20-cm-diameter pipes that are buried to a few meters depth; this is a similar design to most of the monuments used in the EDM network. The measurements are made every 10 min and are telemetered to the USGS in Menlo Park, California. Although the sensor can easily resolve distance changes of less than 0.05 mm (Langbein *et al.*, 1993), the longer-term fluctuations (unpublished data, ftp:// ehzftp.wr.usgs.gov/langbein/CREEP/; Roeloffs, 2001) in the creep data suggest that similar mechanisms of monument instability observed in two-color EDM data are present in the creep measurements.

Langbein *et al.* (2005) presented the initial creepmeter data that span the 2004 mainshock (Fig. 4). Unfortunately, at 6 of the 12 sites, the coseismic displacements were compromised because the slip at these sites exceeded the 25-mm range of the instrument. In most cases, the Invar wire was stretched but not broken, which allowed the instrument to be manually reset by feeding more Invar wire into the displacement sensor and carefully measuring the amount of wire needed to bring the instrument back on scale. However, at one site, XPK1, the wire broke and the measurement of slip could not be achieved. The wire was fixed and the meter was reestablished as XPK2 following the earthquake. All of the Parkfield creepmeters were visited and repaired within four days of the 2004 event. Consequently, because the wires were either stretched or broken, data were lost at several sites during the first few days of the postseismic period. At two of the creepmeter sites with stretched wires, however, XMM1 and XTA1, there are redundant sensors, labeled XMBC and TABC respectively, that have lower sensitivity but greater range. Their data independently confirmed the manual measurements of slip at these sites.

The key observation (Bilham, 2005; Langbein *et al.*, 2005) from the creep data is that, at many of the sites, slip did not occur immediately at the time of the mainshock, but rather, the surface slip became detectable anywhere between 0.5 and 3 hr following the mainshock (Fig. 4a). The exception is XRSW on the SWFZ, where slip was detectable on its first sample made within 5 min of the mainshock. At the four sites, XMM1/XMBC, XMD1, XVA1, and XPK1, the data suggest that slip did occur nearly coincident with the mainshock. One explanation is that the shaking from the earthquake disturbed the instruments and introduced a spurious offset. Evidence of this mechanism is from a record at XMM1 during seismic experiments in 2002 and 2004 where nearby explosions caused an offset in the creep record (Ⓔ see material in the electronic edition of BSSA). On the other hand, these sites are clustered together and also are located above the zone where the inferred coseismic slip is greatest based upon the model developed, described subsequently.

Strain

The borehole strainmeter network was established in the mid-1980s (Johnston *et al.*, 1987, 2006; Roeloffs and Langbein, 1994). Of the initial 12 instruments installed at eight sites, there are seven instruments at five sites that are currently operating. Two different instrument types were installed in boreholes at approximately 200-m depth. One is the Gladwin tensor strainmeter, BTSM, which consists of three extensometers. The other type is the Sacks–Evertson volumetric strainmeter (BSM). Currently, two BTSMs and five BSMs are operating; both BTSMs are colocated, but in separate boreholes, with the BSMs (Fig. 1). These data are processed to remove the signals of the Earth tide and, in the case of BSM, the effect of changes in atmospheric pressure is also removed. Figure 5 shows the time series of strain changes recorded at two BSMs and companion BTSMs that recorded the largest, coseismic signals in this network. (Ⓔ More data are shown in the electronic edition of BSSA). Like the creep data, BSM measurements are made every 10 min and are telemetered to USGS. In addition, 200-samples-per-sec recordings at the BSMs are available (Langbein *et al.*, 2005), but the record is 40 sec long and only covers the seismic shaking (Borcherdt *et al.*, 2006); these data are not considered here. For the BTSM measurements, they are made either at 18-min (DL) or 30-min (FL) intervals and telemetered to USGS.

Results

The data have been examined in two ways: determining the temporal character of the deformation and estimating the distribution of slip consistent with the displacements. With an accurate model of the postseismic response, it is possible to estimate coseismic displacements, and, at a few times when there are SGPS measurements, the postseismic displacements. These displacements are put into a dislocation model for slip on the San Andreas fault. Using a combination of high-rate GPS, the daily solutions from the CGPS network, the infrequently sampled SGPS and EDM data, and constraints of surface slip estimated from the creepmeter data, a model of the coseismic slip distribution and a model of the postseismic slip at 2 months and at 8 months after the mainshock are estimated.
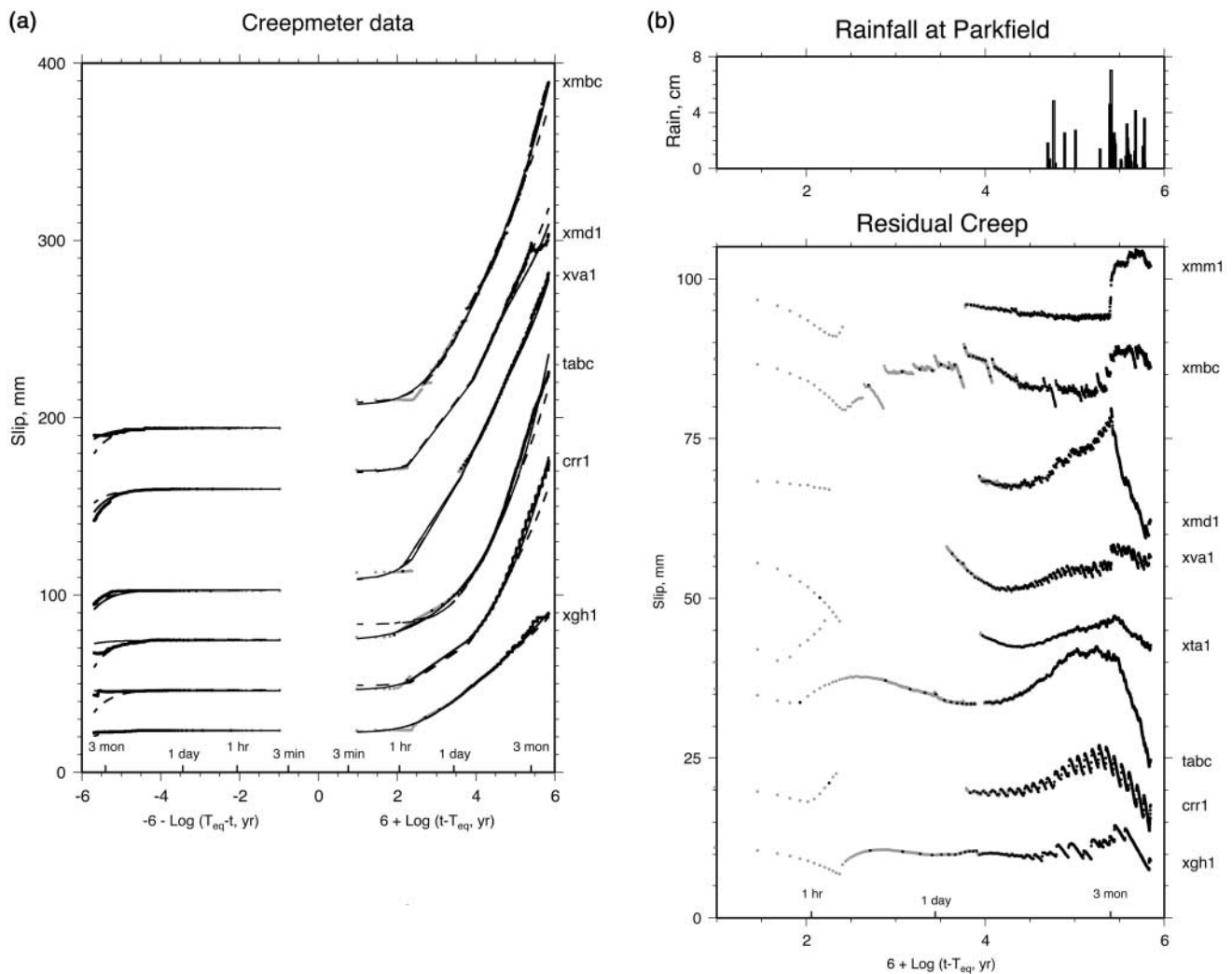
Figure 4. (a) Creepmeter data are shown along with the predicted slip from the modified Omori's law (solid line) and the model of Perfettini and Avouac (2004) (dashed line). The black dots are the creep data sampled at 6-hr intervals, whereas the gray dots are 10-min samples. (b) The residuals for the postseismic interval are shown from fitting Omori's law to the creep data. Rainfall data from Parkfield are shown in the top panel.

Postseismic Deformation

In general, the time-dependent model of equation (1) is fit to the various observations. More detailed analysis is done with the GPS data for several reasons: the sampling rate is between 1 min and 1 day, observations are present within 100 sec of the time of the mainshock, and these data have better long term precision than either strain or creep. In addition, examination of the residuals to the fit of Omori's law to strainmeter data suggests that the strain data still contain additional complexity that, in part, may be attributed to changes in the height of the water table.

GPS. The time-dependent model of equation (1) is fit to each of the three different time series of CGPS data, 1-min, 30-min, and 1-day sampling. The rate and sinusoidal terms are assumed to be zero for the two high-sample-rate sets. For the time-series daily sampling, only the period after the December 2003 San Simeon earthquake (Hardebeck *et al.*, 2004) is selected, and both the rate and annual periodicity are estimated along with the terms of Omori's law (A and τ) and the coseismic offset due to the Parkfield mainshock. In addition to estimating the model parameters, the amplitudes of the noise component are estimated simultaneously using the maximum likelihood method of Langbein (2004). With the high-sample-rate data, the noise model is assumed to be a Gauss–Markov process with an index of -1, following the results found by Langbein and Bock (2004). In addition, flicker noise is assumed for the longest periods in the high-sample-rate data. For the daily data, the noise model is assumed to be a combination of flicker and random-walk noise, which approximates the power-law noise found in
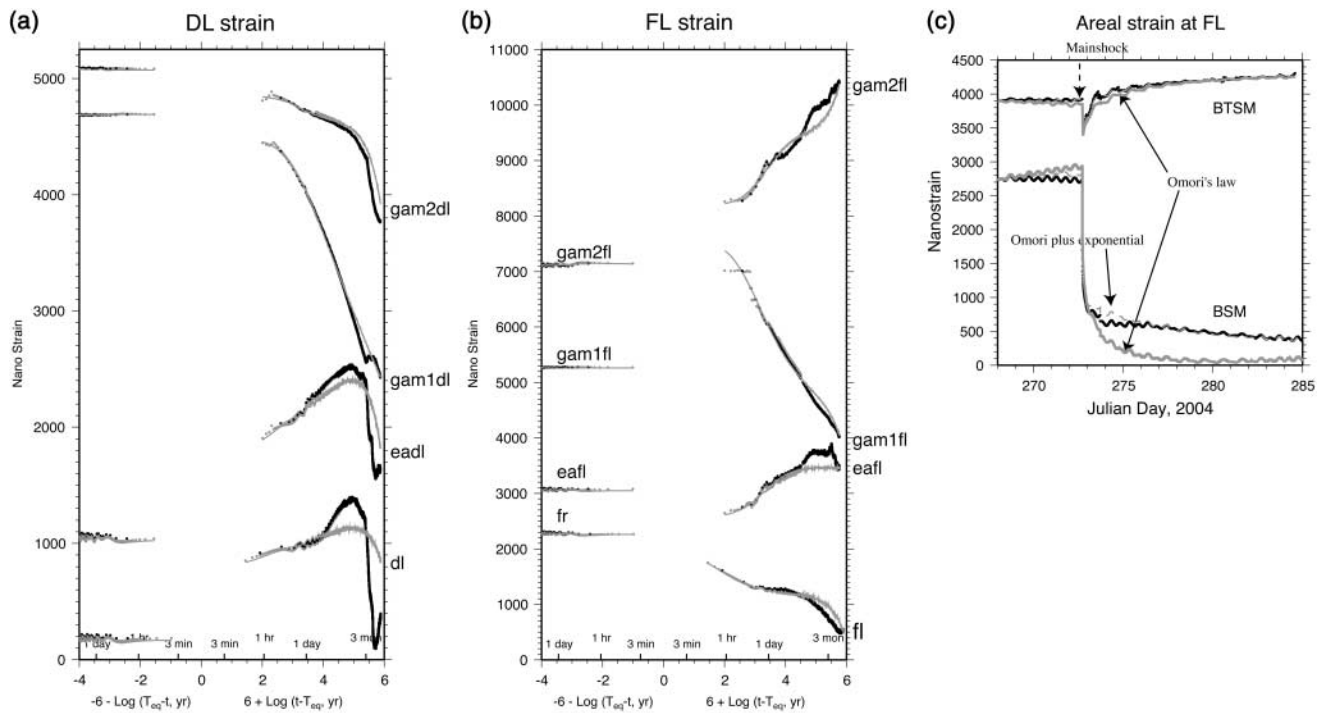
Figure 5.   (a), (b) Strain data from two sites are shown along with the predicted
strain changes from the modified Omori's law (gray line). The black dots are the strain
data sampled at 3-hr intervals, whereas the gray dots are more frequent samples. The
bottom trace, labeled with the site name, is the dilatometer data that have been rescaled
from volumetric strain to areal strain with extension being positive. The second to the
bottom trace is the areal strain from the colocated, tensor strainmeter. The top two
traces are the engineering shear-strain components from the tensor strainmeter. (c) The
times series of the dilatometer and areal strain data for the FL strainmeters during the
coseismic and first 12 days of postseismic deformation. The solid, gray curve is a fit
of Omori's law to these data; the dashed, gray curve is fit of a combination of Omori's
law and an exponential curve.

GPS by Williams *et al.* (2004) when the index is ≤ -1. For
each component, the 1-min, 30-min, and the daily data are
treated separately. Later, we combine all three data sets.

The results illustrate the continuity between the 1-min,
30-min, and daily data (Fig. 2), but the estimate of τ depends
upon the specific time series. For instance, for the east com-
ponent of POMM site, τ ranges between 4 min and 1.5 days.
Thus, both the time of the initial set of observations and the
length of the time series are reflected in the value of τ. In
the case of the north component of POMM, the estimated
value of τ from the 1-min sampled data reflects the delay of
the onset of postseismic deformation.

The modified form of Omori's law (Jeffreys, 1958;
Utsu, 1961) is fit to all of the data from each component to
accommodate the apparent continuity of all three time series
and to reconcile the apparent variations in τ. Typically, the
modified Omori's law has been applied to studying after-
shock rates in the form of $[1 + (t - T_{eq})/\tau)]^{-p}$ (Reasenberg
and Jones, 1989). The modified Omori's law for rate-depen-
dence is integrated to displacement as

$$\frac{A\tau}{1-p}\left[(1 + (t - T_{eq})/\tau)^{1-p} - 1\right]. \qquad (2)$$

The covariances estimated from the first curve-fitting pro-
cedure are used as weights to estimate the parameters of
offset, O, rate, R, Omori amplitude, A, time constant, τ, and
the index, p. The value of p is associated with rate that the
postseismic deformation returns to its background rate; a
larger value of p indicates a more rapid return to the back-
ground rate than a smaller value of p. In most cases of best-
fit curves (Fig. 3; Ⓔ see also the material available in the
electronic edition of BSSA) the index, p, is similar to the
0.8 to 0.9 estimated by P. A. Reasenberg (personal comm.,
April 2005) for the Parkfield aftershock sequence. Of the 22
components where the parameters of the Omori's law could
be reliably estimated, 18 have estimates of $p < 1$ and four
have values of p between 1.0 and 1.3; these values of p are
consistent with other aftershock sequences (Reasenberg and
Jones, 1989). Excluded from this summary are data from
LOWS, because it is located too far from the fault to obtain
good estimates of postseismic displacement, and CARH, be-
cause it could not be fit with Omori's law. Initially, CARH
(Fig. 2) translated to the southeast during the earthquake,
but, postseismically, it was displaced to the northwest.

From the values of A, τ, and p, we can predict two

aspects for the postseismic period: How long will it take for the postseismic rate decrease to be within 1 mm/yr of the secular rate? And, after 2 months and 8 months of measurements, what proportion of the total postseismic deformation does this represent? Because the parameters of Omori's law are estimated for each time series, the predictions span a wide range, but the median time to decay to a 1 mm/yr rate is 8.3 years with interquartile range from 4 to 22 years. Likewise, 2 months of deformation represents 35% (median) of the total postseismic deformation with an interquartile range of 30% to 49%. At 8 months, the total deformation is 47% (median) with an interquartile range of 38% to 60%. Thus, the interval between 2 and 8 months only represents about 10% of the total postseismic deformation. This extrapolation assumes, of course, that postseismic period is governed by a creep process; other processes with different temporal and spatial patterns might come into play at Parkfield, such as poroelastic response and viscous flow in the crust beneath the fault.

Although the modified Omori's law fits the GPS data, it is believed to be unsatisfactory because it does not explicitly test any physical relationship (e.g., Savage *et al.*, 2004). Recently, Perfettini and Avouac (2004) derived the following relation for a one-dimensional, spring and block slider model that exhibits a velocity strengthening friction law and might be related to the mechanism of primary creep in many materials that are suddenly loaded. This relation,

$$A\log[1 + \delta(\exp((t - T_{eq})/t_r) - 1)] \quad (3)$$

is similar to the simple Omori relation when $t - T_{eq} \ll t_r$ where t_r is the relaxation time. In addition, the ratio, t_r/δ, becomes τ in the simplified Omori's law. When $t - T_{eq} \gg t_r$, however, then unlike the Omori's law where rate approaches zero, the aforementioned model predicts that the rate approaches steady state creep of $A/t_r\ln10$.

In most cases, the misfits to the model of Perfettini and Avouac (2004) (Fig. 3, green curve) are not much different than those from the modified Omori's law. In modeling the Perfettini and Avouac (2004) equation, we forced the preseismic rate to the value of $A/t_r\ln10$ on the assumptions that the preseismic rate is the creep rate and that there was no detectable creep prior to the mainshock. Where the model of Perfettini and Avouac (2004) seems to break down is when there is no delay in the onset of postseismic deformation; the north component of MNMC and the east component of POMM (Fig. 3) exemplify the misfit of the Perfettini and Avouac (2004) model to the data.

Recently, Montési (2004) examined another version of the one-dimensional spring and slider block model but, instead of a velocity strengthening friction law, he used a ductile creep law where the slider velocity, V_s, has a power-law relation with the stress, $V_s \sim \sigma^n$. With this constitutive law, he derived the displacement of the slider to be:

$$nV_o\tau_m[(1 + (1 - 1/n)t/\tau_m)^{1/(1-n)} - 1], \quad (4)$$

which is strikingly similar to the modified Omori law (equation 2). Substitution of variables gives $p = 1/(1 - 1/n)$ and $\tau = \tau_m/(1 - 1/n)$. Other than the constitutive law, the other difference between Montési's results and that of Perfettini and Avouac (2004) is that Perfettini and Avouac (2004) included a long-term loading rate, $A/t_r\ln10$, but this could not be included in the analytic result of Montési (2004); instead, Montési (2004) performed numerical simulations that included an external loading rate. Nonetheless, the Montési (2004) model provides a physical basis for the modified Omori's law where n describes the relation between stress and the slider velocity, and τ_m is the ratio between the velocity and acceleration of the slider immediately after the earthquake.

Creep. Both the modified Omori and Perfettini and Avouac (2004) equations are fit to data from the creepmeters that exhibited postseismic slip. Like the GPS, the values of p and τ are similar, with p ranging between 0.7 and 1.3 (Fig. 4). In fitting curves to the creep data, the creep data are broken into two time series, the first of which consists of 10-min samples that span 20 days centered on the time of the mainshock. The 10-min data capture initial postseismic deformation and are influential in estimating τ in Omori's law. The second set consists of 6-hr samples that span the 1.25-year period starting in March 2004. Since the maximum likelihood method of Langbein (2004) is used to estimate the parameters of Omori's law, we assume that the error model of these data is a combination of power law and white noise. We typically find that the power law index is around -2, which corresponds to random-walk noise.

At a few creepmeters, slip occurs as discrete events superimposed on a low rate of slip. Discrete creep events occur regularly at one site, CRR1 (Fig. 4) judging from the residuals from fitting the modified Omori's law to the creep data. By using a logarithmic timescale, it is apparent that the time between successive events is proportional to $\log(T)$. This relation was noted previously by Scholtz *et al.* (1969) at the same site following the 1966 Parkfield earthquake. At the other creep sites, this regularity is not as apparent or as persistent. At XGH1, there appears to be some regularity in the timing of creep events, but after three months of postseismic deformation, the regularity ceased. In fact, the 3-month time corresponds to the onset of heavy, winter-time rainfall for the Parkfield area; the effect of rain is seen in plots of the residuals of the creep data shown in Figure 4b. Previously, others have noted that creepmeters not only respond to fault slip, but also respond to rain (Roeloffs, 2001; Schulz *et al.*, 1983).

Strain. Like the creepmeter data, the modified Omori's law is fit to the tensor strainmeter and the dilatometer data (Fig. 5a,b; Ⓔ see also the material available in the electronic edition of BSSA). The volumetric strain measured by dila-

tometer is rescaled to represent areal strain measured by the nearby tensor instrument. The other tensor components are shown as orthogonal components of shear (Gladwin and Hart, 1985). Like the creep data, the strain data are broken into two time series: one with 10 min (or 18 or 30 min for BTSM) and a second with 3-hr sampling. To first order, the Omori's law appears to describe many characteristics of the data in the postseismic interval. In detail, however, there are problems fitting the observations to this simple model, particularly when the dilatometer data and the tensor strain data for areal component of FL are compared with the coseismic and first 15 days of the postseismic period (Fig. 5c). The key observation is that when the simple Omori's law is fit to both time series, the Omori's law does not satisfactorily fit the dilatometer data. When an exponential function $(1 - \exp(t/\tau))$ is added to the Omori's law, however, then the fit becomes satisfactory. Although the coseismic displacements are similar in size recorded on both instruments at FL, their postseismic responses are opposite in sign (Fig. 5b,c). Finally, the estimates of the index p for the modified Omori's law to the strain data range widely, from 0.95 to 2.0 and, on average, tend to differ from the estimates p for both creep and GPS data; these ranged from 0.7 to 1.3 with most being less than 1.0. For the 11 time series from both sets of strainmeters, four time series yielded $p = 2$, and only two sites had $p < 1$. In fact, high values of p for the strain data indicate a rapid decay in strain rates, much faster than either the Omori rate or Perfettini and Avouac rate that approximate $1/t$.

Thus, first-order interpretation suggests that the strain data are much more complex than can be represented by Omori's law. For example, on many of the time series of strain data, especially those for the BSMs, the rate changes abruptly at three months after the 2004 Parkfield earthquake, corresponding to heavier than normal rainfall at Parkfield, which recharges the local aquifers and changes the loading locally at the strainmeter.

Comparison of Coseismic Offsets from GPS. Coseismic offsets can be independently estimated from either the 1-min, 30-min, or the daily GPS data; however, the term "coseismic offset" needs to be carefully defined. For instance, the east component of POMM has an Omori relation estimated to be $6.4\log(1 + t/0.19)$, where t is the time in minutes from the mainshock. At the time of the mainshock, the Omori contribution is zero, but at 100 sec after the mainshock, the Omori displacement is 6.3 mm. Because of the passage of seismic waves, however, we choose to delete those data from the first 100 sec after the mainshock and therefore cannot confirm whether the 6.3 mm is best characterized with an Omori relation or a simple offset in the data. With the data on hand, the best that we can define as a coseismic offset is the displacement a few minutes after the mainshock, which we select to be 100 sec. Thus, coseismic offsets for the high-rate data are estimated by fitting equation 1 to these data and summing the postseismic slip

evaluated at 100 sec with the coseismic offset O. The coseismic offsets from the daily GPS data are estimated by fitting equation (1) to the observations and simply using the value O.

The coseismic offsets estimated from the daily solutions can be compared with those estimated from the 1-min solutions (Fig. 6). To first order, the offsets estimated 100 sec after the mainshock are roughly 75% of those estimated using the daily solutions. This is a key result; postseismic deformation begins immediately and coseismic displacements estimated from either daily solutions or SGPS data can be biased because they could include postseismic deformation, too.

Fault Modeling

Data. A model of both coseismic and postseismic slip is determined from the displacements measured by GPS and EDM. For the coseismic interval, the displacements estimated at 100 sec after the mainshock are used. For the postseismic interval, we estimate the displacements at 60 and 230 days after the mainshock because those times correspond to occupation by SGPS. Because we lack data for the SGPS sites immediately before the Parkfield earthquake, however, the coseismic and postseismic displacements cannot be reliably estimated. Instead, the total displacement, D_T, which is the coseismic and T_{obs} days of postseismic displacement, is estimated by substitution of $D_T = O + A\log(1 +$
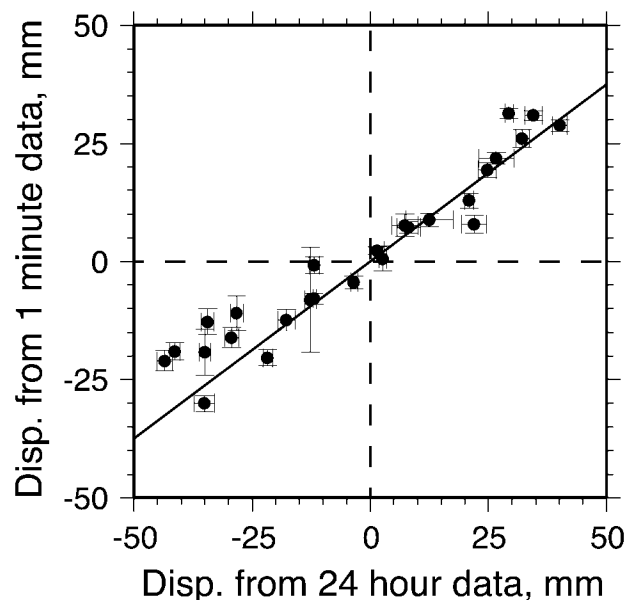

Figure 6.   GPS coseismic displacements estimated from daily data versus the displacement estimated from 1-min data. See text for discussion of how the estimates are derived. The error bars are the one-sigma limit and are estimated by propagating the full data covariance through the least-squares procedure fitting equation (1) to the daily GPS data and separately to the 1-min GPS data.

T_{obs}/τ) into equation (1). This equation works when there are enough data to detect the curvature defined by Omori's law. For the postseismic measurements made only in spring 2004, it is only possible to estimate a rate, defined by the measurements made prior to the mainshock, and an offset that is taken as a sum of coseismic and postseismic displacement 230 days after the mainshock.

Effectively, four sets of data are yielded by GPS and EDM. The coseismic displacements are those estimated from the high-rate GPS measurements discussed previously. A second set consists of a combination of CGPS, EDM, and SGPS measurements made within the first 60 days of the postseismic interval; these measurements are really the sum of the coseismic slip and 60 days of postseismic slip. The third set consists of measurements from SGPS sites and the lone EDM site that were observed in the spring of 2005 but not observed with the first group of measurements made immediately following the mainshock. Finally, a fourth set consists of CGPS, SGPS, and EDM measurements made both 60 and 230 days following the mainshock. Thus, in modeling the coseismic and postseismic slip, each subset of data contains linear combinations of coseismic and postseismic slip with the first set being only the coseismic slip; the second being the sum of coseismic plus 60 days of postseismic slip; the third being the sum of coseismic slip and 230 days of postseismic slip; and the last set being only sensitive to the postseismic slip between 60 and 230 days.

One complication in estimating the rate prior to the Parkfield mainshock is the effect of the San Simeon, **M** 6.5 earthquake in late December 2003. That earthquake generated displacements detectable at all of the CGPS stations in Parkfield (Hardebeck, 2004; Ji *et al.*, 2004; Rolandone *et al.*, unpublished results, 2006) with the maximum displacement being 50 mm at CRBT. Therefore, the San Simeon earthquake also caused unknown offsets at the SGPS stations, because observations were not made at these sites in the period between the time of the two earthquakes. However, by fitting the displacements measured by the CGPS stations to a dislocation model for the San Simeon earthquake with uniform slip that approximates the locus of slip estimated by Ji *et al.* (2004), the predicted displacements at the SGPS stations are used to adjust SGPS data prior to estimating the displacements used for modeling the Parkfield earthquake. Our model of the San Simeon event provides more than 99% reduction in the variance of the coseismic offsets estimated from the CGPS data.

Modeling. The complexity of faulting of the San Andreas is shown by the distribution of seismicity following the Parkfield mainshock (Langbein *et al.*, 2005). In general, the hypocenters of aftershocks are roughly parallel to the surface trace of the San Andreas fault but are offset by 1 to 2 km to the west of its mapped surface. In addition, the aftershock locations indicate that slip at depth is more complex than can be represented by a single plane. More complexity in near-surface faulting is revealed by both the GPS and creep measurements. For instance, the position changes at CARH (Fig. 2) suggest that slip is spread out over a wider fault zone than represented by a single fault plane. In the interseismic period, CARH moved to the northwest in response to fault creep on the nearby San Andreas fault; this fault creep is measured at the creepmeter XTA1 located 0.5 km east of CARH. During the mainshock, however, CARH moved to the southeast, and that motion continued for about one day. Likewise, the creepmeter XTA1/TABC only started to record slip 30 min after the mainshock (Fig. 3). Geologic investigations following the Parkfield earthquake (Langbein *et al.*, 2005; Rymer *et al.*, 2006) and coseismic slip on XRSW indicate that slip occurred on the SWFZ during the earthquake. Measurements from XRSW after the earthquake, however, suggest that the SWFZ only slipped during the mainshock, whereas slip data from the other creepmeters indicate that slip occurred along the main trace of the San Andreas fault after the earthquake.

We model the features of coseismic and postseismic slip that directly affect the geodetic data. These features include the temporal and spatial patterns of surface slip during and after the Parkfield mainshock. Left unmodeled is the complexity of faulting at depth and, to some extent, the distribution of earthquakes west of the main creeping San Andreas fault. Because the spatial resolution of slip at depth tends to be of the order of 5 km or more (Ⓔ see material available in the electronic edition of BSSA), we assume that the geodetic measurements are not particularly sensitive to the details of slip at depth. In an effort to approximate the mapped surface expression of the San Andreas Fault, slip on that fault is modeled as two vertical planes. This is accomplished by offsetting the modeled fault plane by 2 km to the southwest 1 km south of Gold Hill (Fig. 7a). In addition, because coseismic slip was observed on the SWFZ, the SWFZ is included as a third plane. In detail, we model slip on the San Andreas fault from the surface to 16-km depth, but slip on the SWFZ is modeled from the surface to 6 km; because the resolution of slip at depth is poor, it is assumed that any deep slip on the SWFZ merges into slip on the San Andreas fault (Figs. 7a, 8). To simplify the modeling, postseismic slip on the SWFZ is taken to be zero; this assumption is consistent with the creepmeter data. Finally, because we are interested in the spatial distribution of slip, the fault planes are partitioned into many smaller patches each having uniform slip. Each patch is 2 km long horizontally and ranges in width from 0.4 km at the surface to 3 km at depth. Surface displacements for each patch are calculated using Okada (1985).

The distributions of coseismic and two epochs of postseismic slip are estimated simultaneously. The coseismic displacements estimated from the CGPS data are assumed to be proportional to coseismic slip. The cumulative displacements, D_{60} and D_{230}, estimated for both the CGPS and SGPS data are assumed to be proportional to the sum of the coseismic and postseismic slip. Three additional constraints assist with estimating the distribution of slip. Slip at
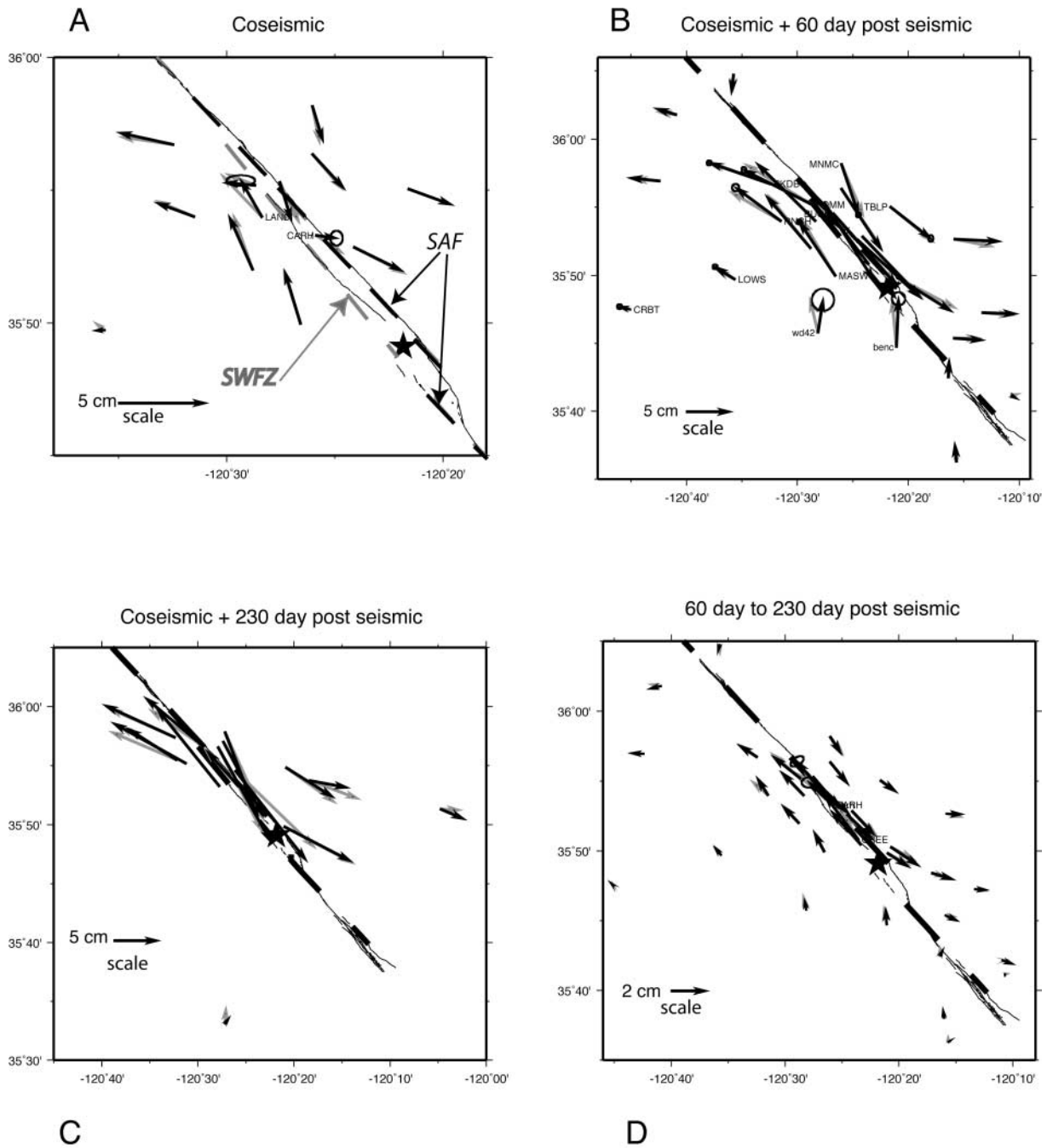
Figure 7. Observed and predicted displacements for CGPS, SGPS, and EDM sites for several episodes spanning the Parkfield earthquake are shown using the model coordinate system of Segall and Matthews (1988). The observed displacements are plotted with black arrows. The predicted displacements are plotted with gray arrows. To simplify the plots, error ellipses (95% confidence) for the observed displacements are only plotted when the residual displacements are greater than two sigma; the site is also named when the residuals are high. The mapped fault trace is a thin line and the modeled fault is a heavy, dashed line. (a) Displacements for the coseismic interval for the CGPS sites. The surface projection of the modeled plane for the San Andreas fault (SAF) is shown with a black, dashed line, while modeled SWFZ is shown with a gray, dashed line. (b) Displacements spanning the coseismic slip and 60 days of postseismic slip; (c) displacements spanning the coseismic slip and 230 days of postseismic slip; (d) displacements spanning the postseismic period between 60 and 230 days.
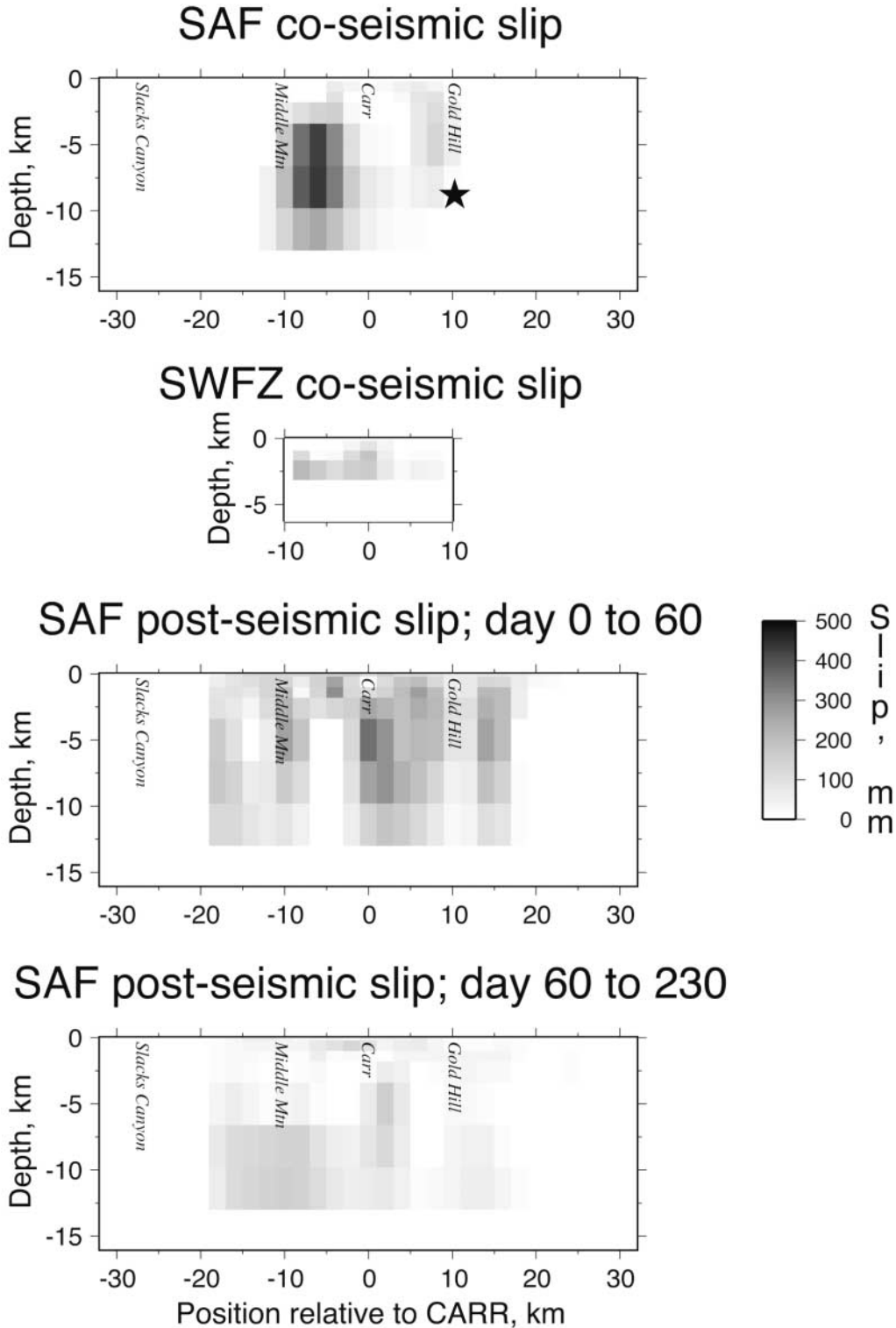
Figure 8. Estimates of distribution of fault slip, in millimeters, during and for two periods after the 2004 Parkfield earthquake on both the San Andreas fault (SAF) and SWFZ. Plots of vertical cross sections of the fault plane looking from the southwest. Geographic locations are indicated on the cross sections, and the star represents the location of the 2004 mainshock.

the edges of the modeled fault plane is assumed to be zero. Both coseismic slip and postseismic slip are constrained to be ≥ 0. And finally, Laplacian smoothing is used. The optimal degree of smoothing versus fitting the data is determined by cross validation (Murray *et al.*, 2001). Creepmeter measurements of surface slip during the coseismic and postseismic epochs are used as constraints in the modeling. Comparison of creepmeter data and nearby alinement array measurements (Lienkaemper *et al.*, 2006) indicate that creepmeter measurements may not capture all of the slip within the fault zone; hence, creep data are used as loose constraints on the surface slip.

Results of the combined inversion for both slip distributions are shown in Figure 8 along with the observed and predicted displacements of the GPS stations (Fig. 7). Coseismic slip is centered beneath Middle Mountain and 12 km northwest of the mainshock. No significant surface slip is detected in our model for the coseismic interval, which is consistent with the absence of coseismic slip on creepmeters. The moment of the modeled coseismic slip distribution is 1.1×10^{18} N m, which is less than the moment estimated in Langbein *et al.* (2005) using only geodetic data but is closer to the estimate of moment of 0.94 to 1.10×10^{18} N m using seismological data (Langbein *et al.*, 2005). Some near-surface slip is modeled for the SWFZ, which is required to satisfy the southwest displacement of CARH during the coseismic interval.

The distribution of slip during the first 60 days of the postseismic interval complements the coseismic slip. Slip propagated to the surface and extended both northwest and southeast of the coseismic slip patch (Fig. 8). The moment of the postseismic slip distribution is 2.0×10^{18} N m, which nearly doubles that of coseismic slip. In addition, the slip 5 km south of Gold Hill appears to be required; if slip south of Gold Hill is held to be zero, then the position changes of the nearby GPS stations are underpredicted.

During the epoch between 60 and 230 days, the moment of the distribution of slip is approximately 0.8×10^{18} N m, indicating a decrease in the rate of slip. The distribution of slip suggests that the fault has partially locked in the 3- to 6-km-depth range. If the moment is fixed at less than 0.3×10^{18} N m, however, then the deeper slip disappears, but this model underpredicts the displacements measured at LOWS, located approximately 15 km from the fault; the evidence of deeper postseismic slip is based on data from LOWS.

This combined model explains 99.6% of the variance of the observations normalized to their error (Fig. 7). None of the residuals is considered excessively large and the residuals lack any obvious spatial pattern. In this model, 303 observations of EDM line-length changes and GPS position changes are used. Excluded are eight observations that we suspect are from sites located within the broader, perhaps 1-km-wide, San Andreas fault zone. Two are from the EDM site MIDD, which are based upon Langbein *et al.*'s (1990) observation that an anomalous interseismic rate is likely within a broad zone of slip. Another SGPS site, MIDE, also

had an anomalous interseismic rate noted by Murray *et al.* (2001). Inspection of the location of SGPS site OQUI in this report reveals that it is located very close to the SWFZ and that our simple model mislocates fault relative to OQUI. Finally, two length changes on a very short EDM baseline, NORE, were anomalous relative to the modeling presented here. From the 303 observations used in the model, the sums of squares of the residuals normalized to the data error is 563, which exceeds the expectation of 303 needed to satisfy the data. We consider this fit to be satisfactory given the assumptions of the modeling, including a homogeneous, elastic half-space invoked for dislocation modeling, the placement of the faults, and the limitations of modeling the error in the data.

Finally, the model resolution is explored in Ⓔ the electronic edition of BSSA. Tests using the same smoothing parameter yielding the model in Figure 8 indicate 5-km spatial averaging along the length of the fault plane for estimating slip at 5-km depth. Vertical averaging for estimating slip at 5 km is skewed with the averaging interval ranging from 3 km to 12 km. Best resolution is obtained for slip patches centered within the core of the CGPS and EDM networks. In addition, slip among the three epochs imaged is well resolved; that is, prescribed slip on a patch of the fault that slips coseismically produces minimal slip on the patches modeling slip at 60 days.

Discussion

Initial analysis by Langbein *et al.* (2005) for the distribution of slip on the San Andreas fault at Parkfield using the displacements estimated from both the CGPS and SGPS had a seismic potency (slip $\times$ area) that was a factor of 1.5 more than that estimated using seismic data. In this report, however, we reconcile this discrepancy by using the high-rate data from CGPS. Our moment, estimated using the coseismic offsets shown in Figure 6, is 1.1×10^{18} N m, and matches the moment estimated from seismic data. On the other hand, Johanson *et al.* (2006), using the same distribution of GPS stations used here and including Interferometry Synthetic Aperture Array (InSAR) data, estimate a coseismic slip distribution with a moment that is a factor of 2 greater than our estimate. Their analysis uses daily GPS data and neglects the postseismic deformation that occurred during the first day following the mainshock. Other examples of the discrepancy between the seismic and geodetic moment estimates exist, including the 1984 Northridge earthquake where the geodetically derived moment (Hudnut *et al.*, 1996) was 20% more than the moment estimated with a mix of seismic and geodetic data (Wald *et al.*, 1996). For the 1999, **M** 7.6 Chi-Chi, Taiwan, earthquake, several investigators (Ma *et al.*, 2001; Wang *et al.*, 2001; Yoshioka, 2001) noted that inversions for coseismic slip that included GPS data yielded seismic moments that were roughly a factor of 2 greater than moments estimated using only seismic data.

Part of the discrepancy between the geodetically and the

seismologically estimated moments may be significant postseismic deformation occurring immediately after the mainshock, in which case, the initial offsets estimated from the geodetic measurements are biased too high. For instance, prior to installation of continuously operating GPS networks, the initial measurements of displacement followed the main-shock by 1 to 2 days because field personnel needed to be deployed. Consequently, the initial measurement could include some portion of the postseismic deformation along with the coseismic deformation. With rapidly expanding networks of CGPS, however, we should be able to discriminate between coseismic and postseismic displacements such that geodetically and seismologically estimated moments should be equivalent.

Our estimate of the coseismic slip distribution and its moment is confirmed by Johnson *et al.* (2006), where they also use the displacements estimated from high-rate GPS. They use a modified version of the GIPSY point-positioning technique (Larson *et al.*, 2003) to estimate the displacements rather than the processing technique that we use (Bock *et al.*, 2000).

Liu *et al.* (2006) estimate a coseismic slip distribution using only seismic data. Their results indicate that the greatest slip occurred beneath Gold Hill, which does not appear consistent with our estimates based solely on GPS. Their report examines many different models estimated from seismic data, and they find that slip beneath Gold Hill is the most robust feature common to all of their models; slip on patches to the northwest on the San Andreas Fault, although present, is less robust in terms of location of slip. By explicitly forcing slip to be close to a value estimated by Liu *et al.* (2006), which we take as 0.5 m at 9 km beneath Gold Hill, we still fit our data and get a slip distribution (Ⓔ see the material available in the electronic edition of BSSA) similar to that shown in Figure 8 but with a greater slip beneath Gold Hill.

Examination of the high-sample-rate data from CGPS at Parkfield reveals significant deformation immediately after the Parkfield mainshock. At some sites near the San Andreas fault 20 mm of postseismic displacement occurred (Fig. 2) within a day following the mainshock. Thus, care is required when using GPS data to estimate the coseismic slip distribution; if those observations encompass a significant amount of time after the earthquake, then the observations could include significant postseismic deformation along with the coseismic displacements. The rapid onset of postseismic slip having a large moment relative to the mainshock may not be applicable to all earthquakes. The Parkfield segment of the San Andreas fault is characterized as a transition zone between being a creeping fault segment to the northwest and a locked segment to the southeast. Thus, the difference in frictional properties between a locked and a creeping fault could be the key element that allows the Parkfield segment to exhibit a large, postseismic response.

One of the main observations from many studies of the postseismic period is that many of the observable features,

including the rate of aftershocks and deformation, obey what is termed Omori's law, where the decay in rate is inversely proportional to the time following the mainshock. Similar behavior, which is known as primary creep, is observed in many materials following a sudden perturbation in stress. The empirical Omori's law is consistent with a model of a one-dimensional, block and spring model exhibiting a velocity-strengthening friction law (Montési, 2004; Perfettini and Avouac, 2004), and this model is regarded as an analog of a fault zone that exhibits stable fault creep. Although Perfettini and Avouac (2004) tested their model against the observed decay of numbers of aftershocks and position changes from GPS observations for the Chi-Chi earthquake, these data had a limited time span between 1 and 200 days. Likewise, Montési (2004) fit his model to several sets of GPS data with postseismic deformation. This limited time span is not unusual for various reasons. Geodetic sampling rates are usually once per day at most, and commonly, these measurements only start a few days following a mainshock as part of the response of the research community to study the earthquake. In principle, earthquake rate observations should start immediately after the main-shock, but, in practice, getting a reliable rate estimate is only possible about 1 to 2 hr after the mainshock, because the larger aftershocks immediately following the mainshock obscure small events and bias the earthquake catalog.

With the high-rate GPS, the borehole strain, and creepmeter measurements following the 2004 Parkfield main-shock, however, we have deformation measurements made within seconds of the mainshock. Where Omori's law has been verified for 2 orders of magnitude in time, we now have observations that span time over 6 orders of magnitude: from minutes to months. Consequently, the empirical Omori's law and the deformation model of Perfettini and Avouac (2004) are rigorously tested. Both the CGPS and the creepmeter data seem to be well characterized by Omori's law. And, in most cases, the model of Perfettini and Avouac (2004) is indistinguishable from Omori's law. Where the model of Perfettini and Avouac (2004) diverges from the data, however, is when the postseismic deformation starts immediately following the mainshock. This is best exemplified in the data from the north component of MNMC (Fig. 3).

Application of Omori's law to the borehole strain data yields a mixed result. To first order, the law seems to work, but other processes seem to be detected by the strain data. For instance, the addition of an exponential curve to assist in characterization of the postseismic strain seems to improve the fit to the data. The strain data appear to be characterized by both an exponential response, suggesting a diffusion process with a 1-day time constant (Fig. 5c), and by Omori's law, suggesting a velocity strengthening mechanism. Whether the exponential character is due to a regional effect or is just local to the strainmeter, however, needs more investigation.

The estimated value of the power law index of the modified Omori's law derived from the GPS and creepmeter data

should provide some insight into the constitutive law that governs slip during the postseismic interval. Our estimates of the Omori index, p, range from 0.7 to 1.3. Evaluating the relation between the index of the ductile creep law, n, using $n = p/(p - 1)$, gives large absolute values on n and they are both positive and negative. For $p = 1$, the value of n is infinite but the Montési (2004) relation becomes a model for velocity strengthening. When $p < 1$, n is negative, which appears to be a nonphysical model of a fault constitutive law. Through simulations, however, Montési (2004) includes some additional loading coupled with positive values of n that produce curves of displacement that, if fit to a modified Omori law, those fits yield an apparent value of $n < 0$. For the example, with $p = 0.9$, figure 4 from Montési (2004) suggests that the additional loading velocity is 5% of the initial sliding velocity with a velocity-strengthening friction law, $(1/n = 0)$. One half of all of our estimates of p from CGPS and creep data range between 0.86 and 1.0, which suggests that additional loading could be occurring on most of the fault at Parkfield. One candidate for the additional load is the interseismic strain accumulation but that is taken into account by the rate, R, in equation (1). Another candidate to reload the shallow part of the San Andreas fault is relaxation of the lower crust or mantle by viscous flow (e.g., Pollitz, 2001). We conclude that a model of velocity strengthening friction with some additional loading of the fault is consistent with our data.

Finally, with the aid of dislocation modeling (Okada, 1985), the position changes measured by GPS, length changes measured by EDM, and surface-slip observations made with creepmeters have been used to infer the spatial distribution of slip in the San Andreas fault zone during the initial postseismic interval. Knowing the distribution of postseismic slip provides some limits on how the perturbation of stress provided by the mainshock redistributes the load and allows parts of the fault that exhibit velocity strengthening to slip. With the addition of postseismic slip to the coseismic slip, the slip-predictable model of earthquake occurrence (Shimazaki and Nakata, 1980) can be tested. The slip-predictable and the time-predictable models are two end members describing the earthquake cycle. Previously, Murray and Segall (2002) demonstrated that the time-predictable model is inconsistent with the geodetic observations spanning the earthquake cycle at Parkfield. In addition, Murray and Langbein (2006) conclude that by 2004, the slip deficit since the 1966 Parkfield earthquake had accumulated at least to 9.3×10^{18} N m. The seismic moment of the mainshock is 1.1×10^{18} N m, which is roughly a factor of 9 too small to be slip predictable.

The 2004 Parkfield earthquake has significant postseismic deformation, however, and from modeling these observations, the moment associated with continued slip of the San Andreas fault is 2.8×10^{18} N m. From extrapolation of Omori's law using the postseismic GPS data, the 8 months of deformation observed represents 50% of the expected postseismic deformation. Thus, over the next 5 to 10 years,

it is expected that the postseismic slip will double and bring the total slip released, with an equivalent moment of 6.7×10^{18} N m, in the Parkfield event closer, but still not enough to match the deficit of slip estimated for the interseismic period. This extrapolation assumes that postseismic creep continues in accordance with velocity strengthening friction law (Perfettini and Avouac, 2004), and that other postseismic mechanisms, such as viscoelastic flow of the lower crust or poroelastic deformation do not occur. These other mechanisms have been seen in other earthquake sequences. On the other hand, Murray and Langbein's estimate (2006) of the moment deficit depends upon the location selected on the fault where the interseismic slip rate is estimated. In estimating the moment deficit for the interseismic period, the section south of Gold Hill was included, but the 2004 event and its postseismic period had little slip on that section. Consequently, the lack of slip south of Gold Hill for both the interseismic and coseismic intervals will bias their assessment of the moment deficit for the entire Parkfield segment, which includes the section of fault both north and south of Gold Hill.

Conclusions

Postseismic deformation is, at the least, the same, if not greater than the coseismic deformation in the 2004 Parkfield earthquake. With the exception of the borehole strainmeter data, the results presented here suggest that, over the timescale between minutes to several months, postseismic displacements follow Omori-type laws similar to aftershock sequences. In fact, postseismic displacement was significant during the first day following the mainshock, so estimates of coseismic displacements may be severely biased if the measurements are temporally undersampled. This bias clearly is the cause of the discrepancy in moment noted by Langbein *et al.* (2005) between the moment derived solely from the geodetic data and the moment that included the seismological data, and it is likely to be a significant factor for the discrepancies in moments calculated for other earthquakes, including Northridge and Chi-Chi. In addition, as suggested by Perfettini and Avouac (2004), the Omori's law in this and other earthquake sequences can be a consequence of a velocity strengthening behavior for a creeping fault.

The geodetic data suggest that most of the coseismic slip is confined at a depth greater than 4 km in a 15-km-long zone centered 5 km northwest of the town of Parkfield and 12 km northwest of the 2004 hypocenter. In the postseismic interval, it appears that slip propagated over a broader section of the fault. Slip has also propagated to the surface where it was measured by creepmeters, to the northwest along the San Andreas fault, and to the southeast past a point beneath Gold Hill and the hypocenter of the 2004 mainshock. The moment estimated for the postseismic slip exceeds that of the mainshock, but, even with extrapolation of the time dependence for deformation, initial analysis suggests that slip through the mainshock and postseismic inter-

val is still less than the accumulated deficit from the inter-
seismic period.

Acknowledgments

References

Bilham, R. (2005) Coseismic strain and the transition to surface afterslip recorded by creepmeters near the 2004 Parkfield epicenter, *Seism. Res. Lett.* **76,** 1–9.

Bock, Y., R. M. Nikolaidis, P. J. de Jonge, and M. Bevis (2000). Instantaneous geodetic positions at medium distances with the Global Positioning System, *J. Geophys. Res.* **105,** 28,233–28,253.

Borcherdt, R. D, M. J. S. Johnston, and G. Glassmoyer (2006). Recordings of the Parkfield 2004 earthquake on the GEOS strong-motion array: implications for earthquake precursors, fault rupture, coseismic and postseismic strain changes, and characteristics of short-period seismic radiation, *Bull. Seism. Soc. Am.* **96,** no. 4B, S73–S89.

Gladwin, M. T., and R. Hart (1985). Design parameters for borehole strain instrumentation, *Pageoph.* **123,** 59–80.

Hardebeck, J., L. J. Boatright, D. Dreger, R. Goel, V. Graizer, K. Hudnut, C. Ji, L. Jones, J. Langbein, J. Lin, E. Roeloffs, R. Simpson, K. Stark, R. Stein, and J. C. Tinsley (2004). Preliminary report on the 22 December 2003 M 6.5 San Simeon, California earthquake, *Seism. Res. Lett.* **75,** 155–172.

Hudnut, K. W., Z. Shen, M. Murray, S. McClusky, R. King, T. Herring, B. Hager, Y. Feng, P. Fang, A. Donnellan, and Y. Bock (1996) Coseismic displacements of the 1994 Northridge, California, earthquake, *Bull. Seism. Soc. Am.* **86,** S19–S36.

Jeffreys, H. (1958). A modification of Lomnitz's law of creep in rocks, *Geophys. J.* **1,** 92–95.

Ji, C., K. M. Larson, Y. Tan, K. W. Hudnut, and K. Choi (2004). Slip history of the 2003 San Simeon earthquake constrained by combining 1-Hz GPS, strong motion, and teleseismic data, *Geophys. Res. Lett.* **31,** no. 17, L17804, doi 10.1029/2004GL020660.

Johanson, I. A., E. J. Fielding, R. Rolandone, and R. Bürgmann (2006). Coseismic and postseismic slip of the 2004 Parkfield earthquake from space-geodetic data, *Bull. Seism. Soc. Am.* **96,** no. 4B, S269–S282.

Johnson, K. M., R. Bürgmann, and K. Larson (2006). Frictional properties on the San Andreas fault near Parkfield, California, inferred from models of afterslip following the 2004 earthquake, *Bull. Seism. Soc. Am.* **96,** no. 4B, S321–S338.

Johnston, M. J. S, R. D. Borcherdt, A. T. Linde, and M. T. Gladwin (2006). Continuous borehole strain and pore pressure in the near field of the 28 September 2004 Parkfield, California, earthquake: implications for nucleation, fault response, earthquake prediction, and tremor, *Bull. Seism. Soc. Am.* **96,** no. 4B, S56–S72.

Johnston, M. J. S., A. T. Linde, M. T. Gladwin, and R. D. Borcherdt (1987). Fault failure with moderate earthquakes, *Tectonophysics* **144,** 189–206.

Langbein, J. (2004). Noise in two—color EDM measurements revisited, *J. Geophys. Res.* **109,** doi 10.1029/2003JB002819.

Langbein, J, and Y. Bock (2004). High-rate real-time GPS network at Parkfield: utility for detecting fault slip and seismic displacements, *Geophys. Res. Lett.* **31,** L15520, doi 10.1029/2003GL019408.

Langbein, J. O, R. O. Burford, and L. E. Slater (1990). Variations in fault slip and strain accumulation at Parkfield, California: initial results using two—color geodimeter measurements, 1984–1988, *J. Geophys. Res.* **95,** 2533–2552.

Langbein, J., E. Quilty, and K. Breckenridge (1993). Sensitivity of crustal deformation instruments to change in secular rate, *Geophys. Res. Lett.* **20,** 85–89.

Langbein, J., F. Wyatt, H. Johnson, D. Hamann, and P. Zimmer (1995). Improved stability of a deeply anchored geodetic monument, *Geophys. Res. Lett.* **22,** 3533–3536.

Langbein, J., R. Borcherdt, D. Dreger, J. Fletcher, J. L. Hardebeck, M. Hellweg, C. Ji, M. Johnston, J. R. Murray, R. Nadeau, M. J. Rymer, and J. A. Treiman (2005). Preliminary report on the 28 September M 6.0 Parkfield, California earthquake, *Seism. Res. Lett.* **76,** 10–26.

Larson, K., P. Bodin, and J. Gomberg (2003). Using 1-Hz GPS data to measure deformations caused by the Denali fault earthquake, *Science* **300,** 1421–1424.

Lienkaemper, J. J., B. Baker, and F. S. McFarland (2006). Surface slip associated with the 2004 Parkfield, California, earthquake measured on alinement arrays, *Bull. Seism. Soc. Am.* **96,** no. 4B, S239–S249.

Liu, P., S. Custódio, and R. J. Archuleta (2006). Kinematic inversion of the 2004 **M** 6.0 Parkfield earthquake including site effects, *Bull. Seism. Soc. Am.* **96,** no. 4B, S143–S158.

Ma, K. F, J. Mori, and S. B. Yu (2001). Spatial and temporal distribution of slip for the 1999 Chi-Chi, Taiwan earthquake, *Bull. Seism. Soc. Am.* **91,** 1068–1087.

Marone, C., C. Scholz, and R. Bilham (1991). On the mechanics of earthquake afterslip, *J. Geophys. Res.* **96,** 8441–8452.

Montési, L. G. J. (2004). Controls of shear zone rheology and tectonic loading on postseismic creep, *J. Geophys. Res.* **109,** doi 10.1039/2003JB002925.

Murray, J. R., and J. Langbein (2006). Slip on the San Andreas fault at Parkfield, California, over two earthquake cycles: implications for seismic hazard, *Bull. Seism. Soc. Am.* **96,** no. 4B, S283–S303.

Murray, J., and P. Segall (2002). Testing time-predictable earthquake recurrence by direct measurement of strain accumulation and release, *Nature* **419,** 287–291.

Murray, J. R., P. Segall, P. Cervelli, W. Prescott, and J. Svarc (2001). Inversion of GPS data for spatially variable slip-rate on the San Andreas fault near Parkfield, California, *Geophys. Res. Lett.* **28,** 359–362.

Okada, Y. (1985). Surface deformation due to shear and tensile faults in a half-space, *Bull. Seism. Soc. Am.* **75,** 1135–1154.

Perfettini, H., and J.-P. Avouac (2004). Postseismic relaxation driven by brittle creep: a possible mechanism to reconcile geodetic measurements and the decay rate of aftershock, application to the Chi-Chi earthquake, Taiwan, *J. Geophys. Res.* **109,** B02304, doi 10.1029/2003JB002488.

Pollitz, F. F., C. Wicks, and W. Thatcher (2001). Mantle flow beneath a continental strike-slip fault: postseismic deformation after the 1999 Hector Mine earthquake, *Science* **293,** 1814–1818.

Reasenberg, P. A., and L. M. Jones (1989). Earthquake hazard after a mainshock in California, *Science* **241,** 1173–1176.

Roeloffs, E. A. (2001). Creep rate changes at Parkfield, California 1966–1999: seasonal, precipitation induced, and tectonic, *J. Geophys. Res.* **106,** 16,525–16,547.

Roeloffs, E. A., and J. Langbein (1994). The earthquake prediction experiment at Parkfield, California, *Rev. Geophys.* **32,** 315–336.

Rymer, M. J., J. C. Tinsley, J. A. Treiman, J R. Arrowsmith, K. B. Clahan, A. M. Rosinski, W. A. Bryant, H. A. Snyder, G. S. Fuis, N. Toke, and G. W. Bawden (2006). Surface fault slip associated with the 2004 Parkfield, California, earthquake, *Bull. Seism. Soc. Am.* **96,** no. 4B, S11–S27.

Savage, J. C., J. L. Svarc, and S-B. Yu (2005). Postseismic relaxation and transient creep, *J. Geophys. Res.* **110,** doi 10.1029/2005JB003687.

Scholz, C. H., M. Wyss, and S. W. Smith (1969). Seismic and aseismic slip on the San Andreas Fault, *J. Geophys. Res.* **74,** 2049–2069.

Schulz, S. S. (1989). Catalog of creepmeter measurements in California from 1966 through 1988, *U.S. Geol. Surv. Open-File Rept. 89-650.*

Schulz, S., R. O. Burford, and B. Mavko (1983). Influence of seismicity and rainfall on episodic creep on the San Andreas fault system in central California, *J. Geophys. Res.* **88,** 7475–7484.

Segall, P., and M. V. Matthews (1988). Displacement calculation from geodetic data and testing of geophysical deformation models, *J. Geophys. Res.* **93,** 14,954–14,966.

Shimazaki, L., and T. Nakata (1980). Time-predictable recurrence model for large earthquakes, *Geophys. Res. Lett.* **7,** 279–282.

Slater, L. E., and G. R. Huggett (1976). A multi-wavelength distance measuring instrument for geophysical experiments, *J. Geophys. Res.* **81,** 6299–6304.

Smith, S. W., and M. Wyss (1968). Displacement of the San Andreas fault initiated by the 1966 Parkfield earthquake, *Bull. Seism. Soc. Am.* **68,** 1955–1974.

Utsu, T. (1961). A statistical study of the occurrence of aftershocks, *Geophys. Mag.* **30,** 521–605.

Wald, D. J., T. H. Heaton, and K. W. Hudnut (1996). The slip history of the 1994 Northridge, Calif., earthquake determined from strong-motion, teleseismic, GPS, and leveling data, *Bull. Seism. Soc. Am.* **86,** S49–S70.

Wang, W.-H., S.-H. Chang, and C.-H. Chen (2001). Fault slip inverted from surface displacements during the 1999 Chi-Chi, Taiwan, earthquake, *Bull. Seism. Soc. Am.* **91,** 1167–1182.

Wdowinski, S., Y. Bock, J. Zhang, P. Fang, and J. Genrich (1997). Southern California permanent GPS geodetic array: spatial filter of daily positions for estimating coseismic and postseismic displacements induced by the 1992 Landers earthquake, *J. Geophys. Res.* **102,** 18,057–18,070.

Williams, S. D. P., Y. Bock, P. Fang, P. Jameson, R. M. Nikolaidis, L. Prawirodirdjo, M. Miller, and D. J. Johnson (2004). Error analysis of continuous GPS time series, *J. Geophys. Res.* **109,** doi 10.1029/2003JB0027412004.

Yoshioka, S. (2001). Coseismic slip distribution of the 1999 Chi-Chi, Taiwan, earthquake deduced from inversion analysis of GPS data, *Bull. Seism. Soc. Am.* **91,** 1068–1087.

Zumberge, J. F., M. B. Heflin, D. C. Jefferson, M. M. Watkins, and F. H. Webb (1997). Precise point positioning for the efficient and robust analysis of GPS data from large networks, *J. Geophys. Res.* **102,** 5005–5017.

U.S. Geological Survey
MS 977
345 Middlefield Road
Menlo Park, California 94025
langbein@usgs.gov